ADVANCED FUNCTIONAL MATERIALS
www.afm-journal.de

Confinement-Induced Phonon Softening and Hardening in Sb_2Te_3 Thin Films

*Julian Mertens, Peter Kerres, Yazhi Xu, Mohit Raghuwanshi, Dasol Kim, Carl-Friedrich Schön, Jonathan Frank, Felix Hoff, Yiming Zhou, Riccardo Mazzarello, Abdur Rehman Jalil, and Matthias Wuttig**

Scaling effects in Sesqui-chalcogenides are of major interest to understand and optimize their performance in heavily scaled applications, including topological insulators and phase-change devices. A combined experimental and theoretical study is presented for molecular beam epitaxy-grown films of antimony-telluride (Sb_2Te_3). Structural,vibrational, optical, and bonding properties upon varying confinement are studied for thicknesses ranging from 1.3 to 56 nm. In ultrathin films, the low-frequency coherent phonons of A_{1g}^1 symmetry are softened compared to the bulk (64.5 cm^{-1} at 1.3 nm compared to 68 cm^{-1} at 55.8 nm). A concomitant increase of the high-frequency A_{1g}^2 Raman mode is seen. X-ray diffraction analyses unravel an accompanying out of plane stretch by 5%, mainly stemming from an increase in the Te-Te gap. This conclusion is supported by density functional theory slab models, which reveal a significant dependency of chemical bonding on film thickness. Changes in atomic arrangement, vibrational frequencies, and bonding extend over a thickness range much larger than observed for other material classes. The finding of these unexpectedly pronounced thickness-dependent effects in quasi-2D material Sb_2Te_3 allows tuning of the film properties with thickness. The results are discussed in the context of a novel bond-type, characterized by a competition between electron localization and delocalization.

1. Introduction

The sesquichalcogenides Antimony-Telluride (Sb_2Te_3), Bismuth-Telluride (Bi_2Te_3) and Bismuth-Selenide (Bi_2Se_3) are characterized by an attractive portfolio of properties, which includes low thermal conductivity, pronounced photon absorption, small effective masses, and topologically protected surface states. These characteristics are employed in phase change (PC)- and thermoelectric applications (TEs) as well as in the design of novel spintronic devices based on their 3D topological insulating (TI) behavior.

This unconventional property combination has recently been attributed to their chemical bonding. Sesquichalcogenides like Sb_2Te_3, Bi_2Te_3, and Bi_2Se_3 utilize an unusual bonding mechanism, coined as metavalent bonding, which differs from conventional covalent, metallic, and ionic bonding.[1,2] It is characterized by a competition between electron delocalization (as in metallic bonding) and electron localization (as in ionic or covalent bonding). This competition and hence the bonding mechanism should be affected if these chalcogenides are present in reduced dimensions, that is, as thin films or small clusters. Hence, we have explored confinement (thickness) effects in thin films of the sesquichalcogenide Sb_2Te_3.

For such films, intrinsic TI performance down to five quintuple-layers (QLs) in Sb_2Te_3 or even two QLs in Bi_2Te_3 was demonstrated by in situ angle-resolved photoemission spectroscopy.[3,4] Based on the successful synthesis of Bi_2S_3 nanosheets, recent density functional theory (DFT) studies considered orthorhombic Sb_2X_3 and Bi_2X_3 (X = S, Se, Te) monolayers as promising candidates for broadband and polarization-sensitive photodetectors and proved their dynamical and thermal stability.[5–7] In those thin films, quantum confinement effects are expected and indeed have already been systematically studied in few quintuple nanoplatelets of Bi_2Se_3.[8] There, asymmetric Raman line shapes have been ascribed to quantum interference effects between discrete high symmetry phonon states and an electronic continuum. A distinct softening of Longitudinal optical (LO) -phonons was observed, which decreased with increasing thickness D more slowly ($\Delta\omega \approx 1/D$) than expected for pure

J. Mertens, P. Kerres, Y. Xu, D. Kim, C.-F. Schön, J. Frank, F. Hoff, Y. Zhou, M. Wuttig
I. Institute of Physics (IA)
RWTH Aachen
Sommerfeldstraße 14, 52074 Aachen, Germany
E-mail: wuttig@physik.rwth-aachen.de

P. Kerres, M. Raghuwanshi, A. R. Jalil, M. Wuttig
Peter Grünberg Institute - JARA-Institute Energy Efficient Information Technology (PGI-10)
Forschungszentrum Jülich GmbH
Wilhelm-Johnen-Straße, 52428 Jülich, Germany

R. Mazzarello
Dipartimento di Fisica
Sapienza University of Rome
P.le Aldo Moro 5, Rome 00185, Italy

The ORCID identification number(s) for the author(s) of this article can be found under https://doi.org/10.1002/adfm.202307681

DOI: 10.1002/adfm.202307681

quantum interference effects ($\Delta\omega \approx 1/D^2$). The reason for this deviation and thus, the main cause of LO phonon softening remains obscure.

This study exemplarily focuses on Sb_2Te_3 thin films grown by molecular beam epitaxy (MBE) in a range between 1.3 and 56 nm. Consequently, confinement effects have to be considered. In a recent study, an unusual thickness-dependence of film properties has already been reported for the monochalcogenide Germanium Telluride (GeTe).[9] Such monochalcogenides are characterized by a number of unconventional properties, too. They possess a moderate electrical conductivity ($\sigma \approx 10^2 - 10^4$ S cm^{-1}), a large optical dielectric constant ($\epsilon_\infty > 15$), large Born effective charges ($Z^* \approx 5 - 8$) and large Grüneisen parameters ($\gamma > 3$). These properties have been attributed to their unconventional bonding.[2,10,11] For this bonding mechanism, a pronounced thickness dependence of properties is expected. Indeed, pronounced changes in atomic arrangement as well as optical and vibrational properties were found for GeTe films as a function of film thickness.[9] Thus, discussing confinement effects from a bonding perspective could be a promising approach to understand application-relevant property changes in sesquichalcogenides, too.

Usually, sesquichalcogenide compounds are treated as van der Waals (vdW) materials.[12] This nomenclature assumes that the interlayer coupling between adjacent quintuple blocks is mediated by weak vdW bonds. Yet, this wording is misleading. A study on strain-engineering of Sb_2Te_3/GeTe superlattices clearly distinguished the sesquichalcogenide compounds from ordinary vdW systems like transition metal dichalcogenides (e.g., $MoSe_2$, $MoTe_2$, WSe_2, $FeTe_2$), the latter of which has attracted growing attention due to their spin-sensitive filtering capabilities in novel electronic devices.[13,14] In most sesquichalcogenides, the coupling between quintuple layers (QLs) is significantly stronger than expected for vdW bonding. As a consequence, the spacing of these gaps is significantly smaller. Both observations provide evidence for a bonding mechanism that exceeds weak vdW bonding. Furthermore, a detailed scanning transmission electron microscopy study on the stacking faults of layered chalcogenides linked the perfect ordering with full crystallographic symmetry found in MBE-grown Sb_2Te_3 thin films to its pronounced interlayer coupling.[15] On the contrary, hexagonal Ge_4Se_3Te exhibits a large number of planar stacking faults due to its much weaker vdW type interlayer coupling.

Consequently, the sesquichalcogenides mentioned above should behave very differently from pure 2D systems like graphene when confined to the nanoscale. In few layer graphene (FLG), the close relation between electronic properties and layer index is used to rapidly determine the layer number of AB-stacked FLG by Raman spectroscopy of the 2D band.[16] However, changes in the Raman signal between four and five layers are already hard to distinguish, different for Bi_2Se_3 nanoplatelets, where thickness-dependent changes of the Raman signal of the $A_{1g}{}^1$ phonon mode remain up to more than ten QLs.[8]

We have thus studied the thickness dependence of optical phonons in Sb_2Te_3 films through time-resolved reflectance changes upon illumination with femtosecond laser pulses, which causes coherent phonon excitation. Interestingly, the literature on coherent phonon excitation on ultrathin Bi_2Te_3 thin films yields conflicting results. While the absence of coherent phonons in thin films up to 10 nm thickness was reported, their observation in nano-confined structures, yet without any confinement effect has been observed.[17,18] Therefore, we investigate the corresponding Transversal optical (TO) phonon-mode in ultrathin Sb_2Te_3 films by means of femtosecond-laser coherent phonon excitation using a common reflection type two-color pump-probe experiment (pump: 800 nm, probe: 520/635 nm).

Femtosecond laser pulses offer an efficient way to simultaneously excite and detect coherent optical phonons in reflection type pump-probe experiments.[19] In this scheme, two femtosecond laser pulses are used: a high intensity "pump"-pulse optically excites the sample while a weaker "probe"-pulse measures the reflectivity of the excited state with a certain delay. Transient reflectance traces with sub-picosecond temporal resolution are obtained. In strongly absorbing materials, a temporally confined pump pulse ($\tau < 100$ fs) can generate coherent optical soft phonons in the THz range by the displacive excitation of coherent phonons (DECP). This optical excitation mechanism is closely related to impulsive stimulated Raman scattering.[20,21] Exploiting the dependence of the sample reflectivity R on the density of optically excited carriers n_e and the phonon-mode related atomic positions Q for moderate pump fluencies

$$\frac{\Delta R(t)}{R_0} = \frac{1}{R_0}\left[\left(\frac{\partial R}{\partial n_e}\right) n_e(t) + \left(\frac{\partial R}{\partial Q}\right) Q(t)\right] \quad (1)$$

allows a precise coherent phonon mode quantification by means of femtosecond real-time reflectivity measurements.[20]

Subsequently, confinement-induced trends with increasing film thickness in the coherent phonon measurements are related to changes in the atomic arrangement. This arrangement of the atoms has been investigated by comparison of X-ray diffraction (XRD) measurements and 1D kinematic diffraction simulations without laser excitation. The experimental study is supported by Density Functional Theory (DFT) simulations focusing on thin-film structure and bonding-related material properties upon changing confinement (film thickness).

2. Results

2.1. Coherent Phonon and Raman Spectroscopy

Transient reflectance data of Sb_2Te_3 are obtained for various thin films ranging from 1.3 to 56 nm. The pump-probe measurements are performed in isotropic and anisotropic (electro-optic sampling) configuration at constant pump fluency.[22] **Figure 1**a exemplarily shows the transient anisotropic reflectance for the Sb_2Te_3 thin film of 6.6 nm thickness. As evidenced by the Fourier-transform shown in the inset, oscillations of two distinct frequencies contribute to the oscillatory behavior and can be identified as coherent phonons of $A_{1g}{}^1$ and $E_g{}^2$ symmetry.[23] Due to the temporal resolution of the pump-probe setup, no indication of the high-frequency $A_{1g}{}^2$ mode is present in the data. To determine the frequency and lifetime of the coherent phonons, we fit the time-domain data to the following empirical equation.

$$\frac{\Delta R_{EO}}{R_0} = \sum_{A_{1g},E_g} Ce^{-kt} \cdot \mathrm{Cos}[\omega t + \varphi] + \sum_{l=1}^{3} C_l e^{-k_l t} \quad (2)$$

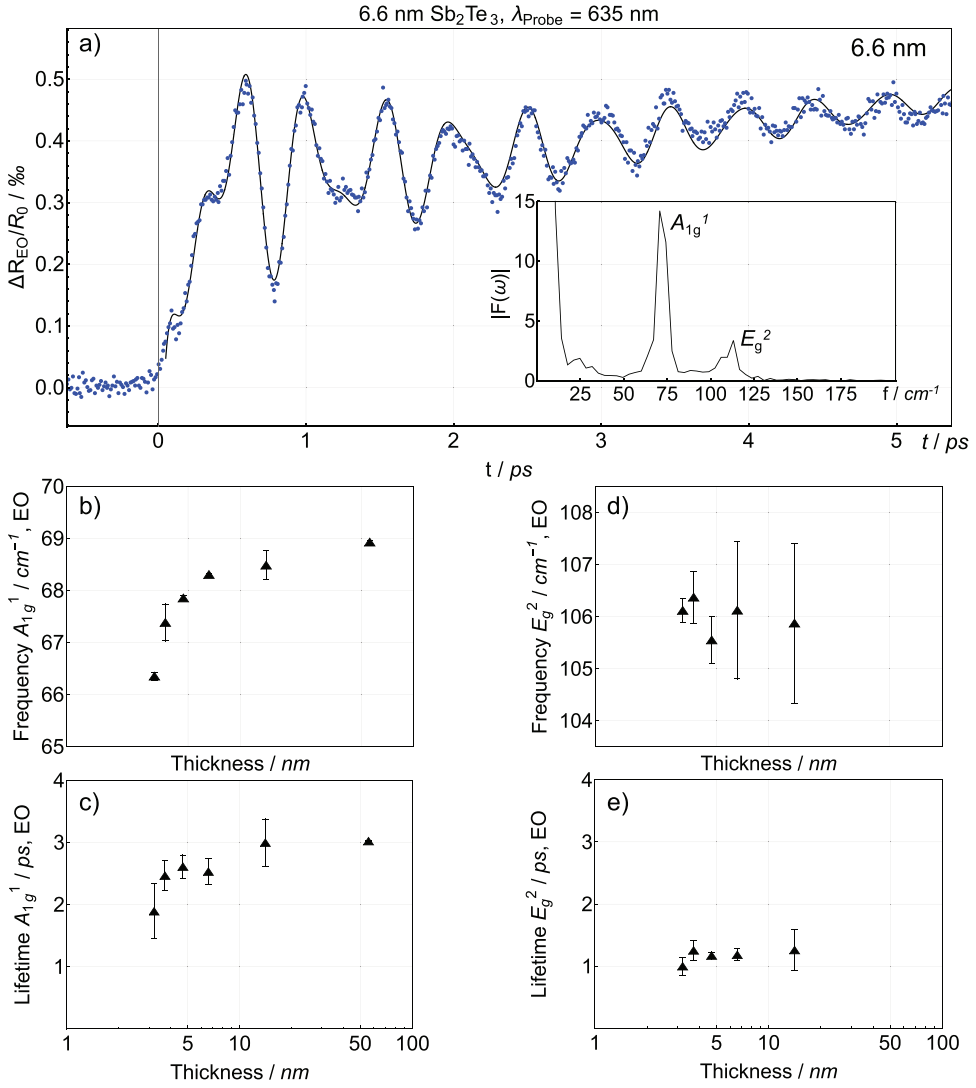

Figure 1. a) Results of transient anisotropic reflectance (electro-optic sampling) exemplarily shown for the 6.6 nm Sb_2Te_3 thin film. The corresponding fit includes two damped harmonic oscillations. In electro-optic sampling, the isotropic transient reflectance is reduced while anisotropic changes are highlighted. This enables the detection of E_g-symmetric phonon modes as shown by the Fourier spectrum in the inset. The frequency and lifetime of the $A_{1g}{}^1$ phonon mode are shown in (b,c). The corresponding values for the $E_g{}^2$ mode are shown in (d,e). In the thickest sample, the contribution of the $E_g{}^2$ mode is too weak to be properly captured by the fit. While the frequency and lifetime of the totally symmetric $A_{1g}{}^1$ mode drop with decreasing film thickness, no trends are observable for the in-plane $E_g{}^2$ mode. The $A_{1g}{}^2$ mode is not resolved due to the temporal resolution of the setup. Errors are based on the fitting of multiple data sets.

including the damped harmonic oscillation at frequency ω and scattering rate k of $A_{1g}{}^1$ and $E_g{}^2$ symmetric coherent phonons with oscillation amplitudes C. In addition, three contributions are included to describe the response toward electronic excitation and deexcitation, as well as a certain amount of lattice heating with distinct amplitudes C_l and scattering rates k_l. Based on fits according to Equation (1), coherent phonon modes are analyzed. The observed coherent oscillations agree well with those reported in literature.[24,25] Clear thickness-dependent trends can be deduced. As shown in Figure 1b, the out-of-plane $A_{1g}{}^1$ mode frequency distinctively drops with decreasing film thickness. A concomitant decrease in coherent phonon lifetime is shown in Figure 1c. Regarding the in-plane $E_g{}^2$ coherent phonon mode, no clear thickness trends are observable as shown in Figure 1d,e.

Transient reflectance traces, measured on different sample spots, are very reproducible. To determine the uncertainties shown in Figure 1, multiple pump-probe traces have been recorded for each sample.

Coherent $A_{1g}{}^1$ phonon softening is confirmed by transient isotropic pump-probe data featuring totally symmetric phonon modes exclusively. The corresponding phonon frequency for each sample is shown in **Figure 2**a. Raw data and fits are available in the Supporting Information (Figure S2, Supporting Information).

A clear drop in coherent phonon frequency is observed with decreasing film thickness. The thickness-dependency starts at around 10 nm. The phonon frequency of the thinnest sample (1.3 nm) is about 5% smaller than the extrapolated bulk value of

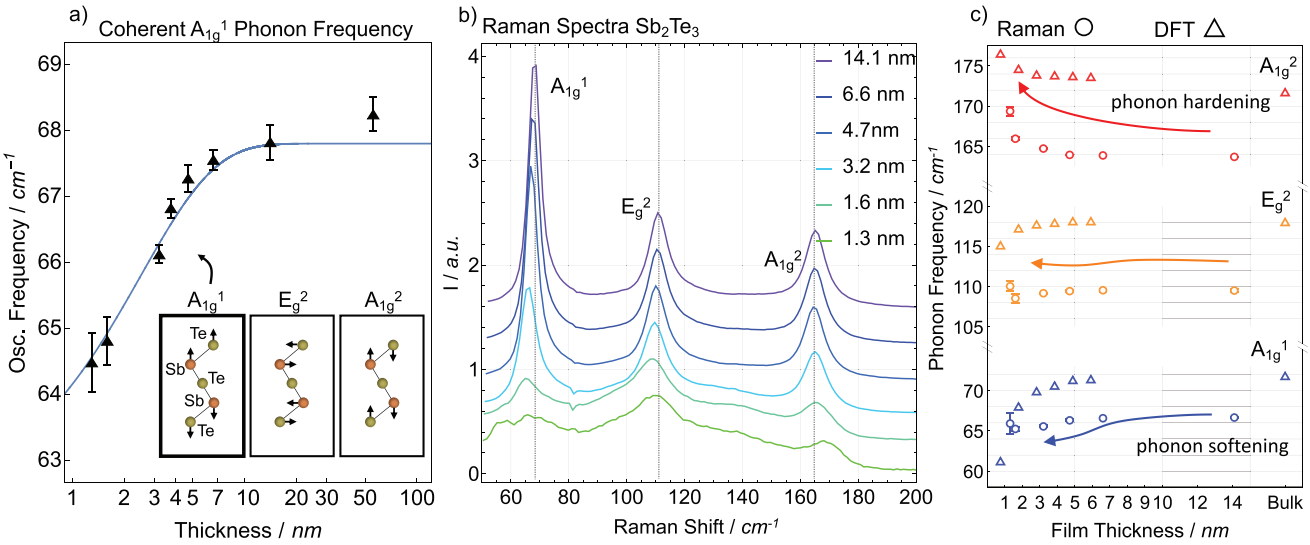

Figure 2. a) Coherent phonon frequency dependence on film thickness obtained from isotropic transient reflectance. A significant drop of the A_{1g}^1-frequency from the bulk value of 68 1 cm^{-1} is observed with decreasing film thickness. The blue line is a guide to the eye. Inset: Ionic displacement pattern of the Raman-active phonon modes observed. b) Raman spectra obtained from various thin film samples. Each curve is normalized to the peak intensity of the E_g^2 mode and vertically shifted for clarity. Vertical lines describe the Raman shift peak positions of the 14.1 nm film, facilitating the identification of thickness trends. c) Thickness dependence of the Raman shifts of the out-of-plane (A_{1g}^1, A_{1g}^2) and in-plane (E_g^2) modes obtained by Lorentzian curve fitting. The distinct coherent phonon softening is confirmed by Raman data of the A_{1g}^1 mode. While no pronounced thickness-dependent trends can be found for the E_g^2 phonon mode, a clear increase in the A_{1g}^2 frequency toward ultrathin films can be identified. The phonon frequencies obtained by DFT calculations, also depicted in the plot, exhibit similar trends.

68 cm^{-1}. The drop in coherent phonon frequency is accompanied by a decrease in the phonon lifetime (see Figure S1, Supporting Information). To confirm the observed thickness-related trends of the A_{1g}^1 phonon mode, Raman spectroscopy measurements at an excitation wavelength of 530 nm have been performed. Figure 2b shows the corresponding spectra for various thin films. The Raman spectra contain three distinct peaks at around 66, 109, and 165 cm^{-1} and can be identified as the A_{1g}^1, E_g^2, and A_{1g}^2 phonon modes, respectively.[23] The E_g^1 mode at a frequency of 40.7 cm^{-1} is not resolvable with the Raman setup utilized. The dashed vertical lines in Figure 2b mark the Raman shift peak positions of the 14.1 nm sample. Figure 2c depicts the Raman shift peak positions of each of the three phonon modes as a function of film thickness. Very similar to the study of coherent phonons, Raman spectroscopy reveals a univocal A_{1g}^1 phonon mode frequency decrease of 2.5% comparing the two thinnest samples to the bulk limit. While the in-plane E_g^2 phonon mode does not exhibit a distinct film thickness dependency, the high-frequency A_{1g}^2 mode hardens with decreasing film thickness. The uncertainties presented in Figure 2c arise from the Lorentzian curve fittings. Additionally, Figure 2c shows the phonon frequencies obtained by DFT (PBE+D2; PBE, Perdew, Burke, and Ernzerhof) calculations for film thickness up to 6 nm, which corresponds to 6 QLs. The data points are obtained by averaging over the frequencies of the relevant A_{1g}^1, E_g^2, or A_{1g}^2 modes. The simulations can adequately reproduce the softening of the A_{1g}^1 modes and the hardening of the A_{1g}^2 modes.

To investigate the microscopic origin of the observed confinement-related phonon-mode shifts, the following section focuses on the atomic arrangement in Sb_2Te_3 ultrathin films studied by XRD experiments.

2.2. Investigation of the Atomic Arrangement

2.2.1. XRD Analysis

Starting from the experimental θ–2θ diffractograms shown in **Figure 3**a, the epitaxial nature of the thickness series of Sb_2Te_3 films is visible as only (00.3n) peaks are present in all films. In addition, reflection high energy electron diffraction (RHEED), in situ acquired during film growth (cf. Figure S6b, Supporting Information), reveals crystalline growth as soon as the film deposition starts. Laue oscillations are present in all films except for the 55.8 nm sample, with an oscillation period corresponding to the film thickness. This confirms that the films contain no grain boundaries parallel to the surface enabling a single coherent optical response (i.e., coherent phonon generation) from the whole thin film. Reciprocal space maps, Angular RHEED and Phi scans in Figures S6–S10, Supporting Information confirm the biaxial texture of the films, similar to the work of Boschker et al.[26] Regarding the 55.8 nm sample, the growth mode has shifted from epilayer growth in the beginning, toward spiral growth along a screw dislocation, which promotes formation of a triangular pyramid aligned to the substrate surface. Images of this sample compared to thinner films are shown in Figures S4 and S5, Supporting Information. This growth mode has already been reported for Sb_2Te_3 and Bi_2Se_3 films.[27,28] The deviation of parts of the film from the substrate alignment can also be seen in the reciprocal space maps in Figure S9, Supporting Information. Since the roughness of the thickest film is still below 10% of the film thickness and the overall amount of mosaic patterns remains low, totally symmetric coherent phonons can be observed even in this sample.

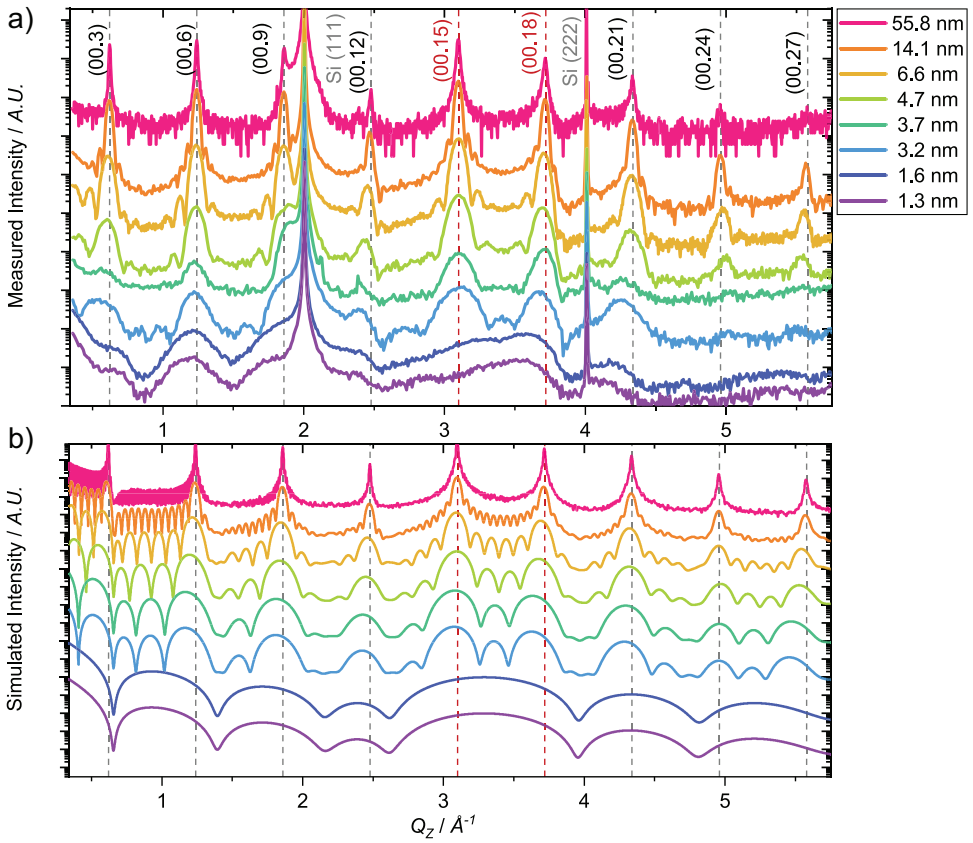

Figure 3. a) θ–2θ XRD data of the thin film series investigated. The films grow epitaxially along the (00.3n) direction. The existence of Laue oscillations for all, except for the thickest sample, is indicative of smooth and coherent growth. Peak shifts toward lower Q values indicate an increase in the c–axis for the thinnest samples. For a detailed discussion of these shifts, kinematic simulations are shown in b).

Considering the experimental θ–2θ diffractograms, diffraction peaks broaden upon decreasing film thickness and most peaks shift to lower Q values. However, not all peaks shift downward, the (00.15) and (00.18) peak positions do not shift or even increase for ultrathin films. Both effects can be explained by studying the 1D kinematical XRD-simulations shown in Figure 3b In these simulations, film growth starts with a full quintuple. The thickest films are well described by bulk conditions, that is, a repeating unit cell containing QLs separated by pseudo vdW-gaps. Considering a single quintuple (thinnest film), no gap is present in the structure, and the corresponding diffraction condition changes. For films in between both edge cases, this results in a continuous merging of the (00.15)–(00.18) and (00.24)–(00.27) peaks when thin films are scaled down toward a single quintuple. Thus, the good agreement between theory and experiment gives evidence that the film growth indeed starts with a full QL and hence a gap at the substrate-interface as expected from Sb:Si surface without dangling bonds.

In **Figure 4**, the thickness dependence of the in-plane and out-of-plane lattice constants of the Sb_2Te_3 films is plotted. The c-lattice constant is determined from the peak positions of the θ–2θ diffractograms shown in Figure 3. The in-plane lattice constant a is measured from XRD peaks with an in-plane component and from evaluation of the RHEED images. Thickness-dependent trends for both lattice constants are visible: the

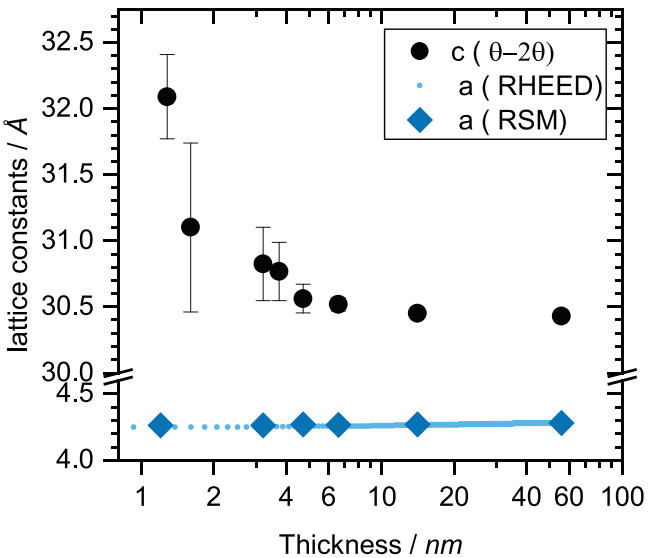

Figure 4. In-plane (a) and out-of-plane lattice constant (c) for different film thicknesses determined by XRD and RHEED analysis. The ultrathin films show a distinct increase in the c-lattice constant up to 5% compared to bulk, while the lattice constant a is compressed by roughly 0.5%.

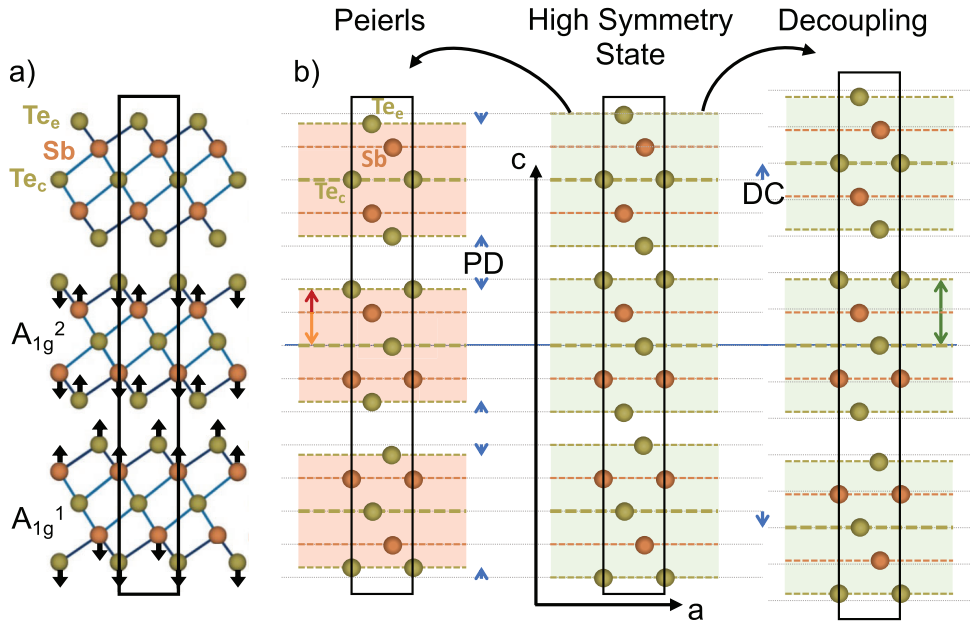

Figure 5. a) Bulk structure of Sb_2Te_3. The rhombohedral unit cell is indicated by the black rectangle. Black arrows describe the $A_{1g}{}^1$ and $A_{1g}{}^2$ -phonon mode displacement patterns. b) Definition of Peierls and decoupling motif used to quantify different distortions along the *c*–axis. In the high symmetry state, no separation between quintuple blocks exists as each $z = const.$ atomic layer lies on the high-symmetry (0015)-planes separated by c/15 (light grey lines). On the right, the Te-Te gap stems from a "decoupling" of quintuple blocks without affecting the atomic plane distances within the block. Contrary, the Peierls motif, shown on the left, is defined as a shift of the outer Te atoms with respect to the high symmetry planes. The corresponding shifts of atomic planes (PD and DC) are represented by blue arrows.

c-lattice constant increases for ultrathin films, while the *a*-lattice constant slightly decreases.

To understand the observed coherent phonon softening in terms of changes in the atomic arrangement, it is essential to gain insights into the underlying distortions within the unit cell. This is especially important for the *c*–axis, as this is the direction of the atomic displacement of the out-of-plane $A_{1g}{}^1$ and $A_{1g}{}^2$ phonon modes which exhibit pronounced thickness dependence. To quantify such distortions within the unit cell, we define two distinct motifs as shown in **Figure 5**b. In a virtual high symmetry state, each atomic layer defined by $z = const.$ is aligned to the high symmetry planes equally spaced at $c/15$. Thus, in the high symmetry state, there is no distinct gap formed at the outer Te sites. Upon increasing decoupling, quintuples shift away from each other without affecting the atomic plane distances within each quintuple block. The corresponding absolute QL shift is called DC. Contrary, the Peierls distortion is defined as the shift of the outer Te atoms with respect to the high symmetry planes and is labeled PD. Consequently, PD is a measure of the distortion within the quintuple. Both distortion types cause the formation of quintuple blocks where the central Te-planes remain on the (0015)-planes. In the following, two different coefficients will be used to quantify the distortion motifs:

$$C_{\text{Peierls}} = \frac{\frac{c}{15}}{\frac{c}{15} - \text{PD}} \overset{\text{DC}=0}{\rightarrow} \frac{d_{\text{Sb-Te}_C}}{d_{\text{Sb-Te}_E}} \tag{3}$$

$$C_{\text{Decoupling}} = \frac{\frac{c}{15} + \frac{4}{5}\text{DC}}{\frac{c}{15} - \frac{\text{DC}}{5}} \overset{\text{PD}=0}{\rightarrow} \frac{d_{\text{Te}_E-\text{Te}_E}}{d_{\text{Sb-Te}_C}} \tag{4}$$

Following this definition, the high-symmetry state is defined by $C_{\text{Peierls}} = C_{\text{Decoupling}} = 1$. The Sb_2Te_3 bulk structure shown in Figure 5a exhibits a combination of both distortions and is uniquely defined by four parameters: The Peierls- and decoupling coefficients C_{Peierls} and $C_{\text{Decoupling}}$ and the lattice parameters a and c. However, to parametrize the arrangement of atomic planes perpendicular to the *c*–axis, the in-plane lattice constant *a* is not required.

To distinguish both types of structural distortions in the different thin-film samples, it is necessary to understand how these distortions affect the XRD patterns. Any shifts of atomic positions in the unit cell change the structure factor and in turn, the peak intensities detected. Exploiting this relation, a systematic study of 1D-kinematic XRD simulations for the different film thicknesses has been performed. **Figure 6**a shows several simulated diffraction patterns with varying amounts of decoupling and Peierls coefficients in comparison with the experimental data of the 14.1 nm sample. The corresponding experimentally determined peak intensity ratios integrated from reciprocal space maps are shown in the diagrams in Figure 6b,c. To obtain the distortion coefficients of the various thin films, simulated (see Figure S11, Supporting Information) and experimentally determined peak intensity ratios are compared (Figure 6d). The resulting distortion coefficients are presented in Figure 6e and corresponding trends of atomic plane distances are shown in Figure 6f.

A proper determination based on experimental diffractograms is possible for each sample except for the two thinnest films. The comparison between experiment and theory yields distinct thickness trends: The decoupling coefficient increases with decreasing

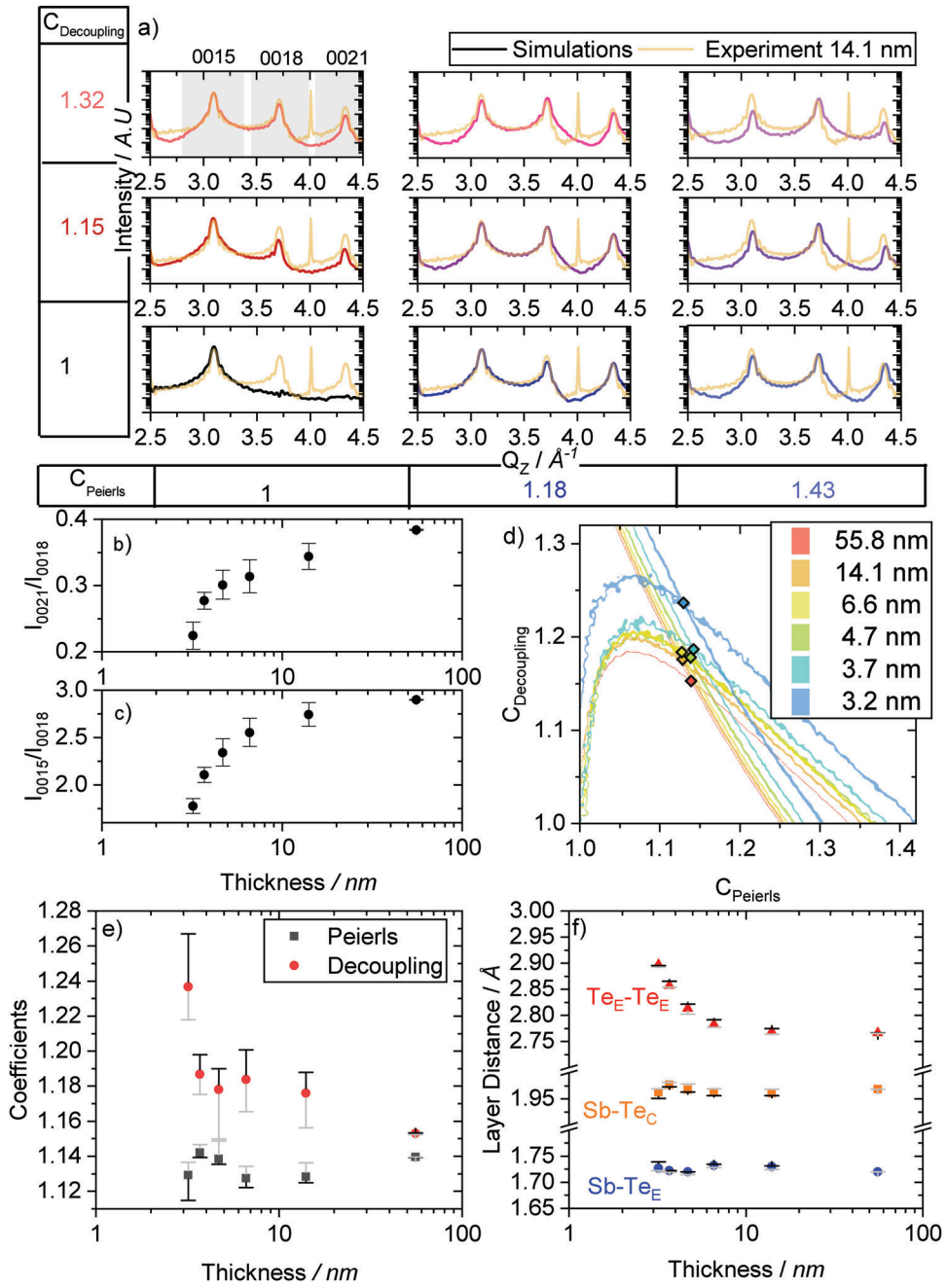

Figure 6. a) XRD-patterns kinematically simulated for different amounts of decoupling and Peierls coefficients and decoupling compared to experimental data (light orange) exemplified by the 14.1 nm film. The sharp peak at around 4.0 $Å^{-1}$ stems from the Si(111)-substrate. Experimentally determined peak intensity ratios b) 15/18 and c) 21/18 for the various thin-film samples. Both intensity ratios distinctively drop as the samples get thinner. d) Numerical determination of distortion coefficients for various thin film samples. e) Thickness-dependence of Peierls and decoupling coefficients. Upon decreasing film thickness, quintuples gradually decouple, while no distinct trend is discernible for the Peierls coefficient due to experimental uncertainties. f) Thickness-dependence of atomic plane distances. The increasing lattice constant can be explained by the increase of the pseudo-van der Waals gap, while a small distortion within the quintuple is visible as well. The black and grey error bars represent the evaluation of d) the lower/upper confidence values from (b) and (c).

film thickness: it increases by roughly 10% comparing the 3.2 nm Sb_2Te_3 film to the bulk state. Unfortunately, due to the limited resolution of experimental data and the numerical methods employed, potential thickness-dependent trends of the Peierls coefficient cannot be identified.

The uncertainties on the coefficients are correlated, denoted by the different colors of the error bars. However, for the evaluation of the atomic layer distances from the simulated coefficients and measured lattice constants, the effect of the correlation is mitigated. Figure 6f shows the interatomic layer distances obtained

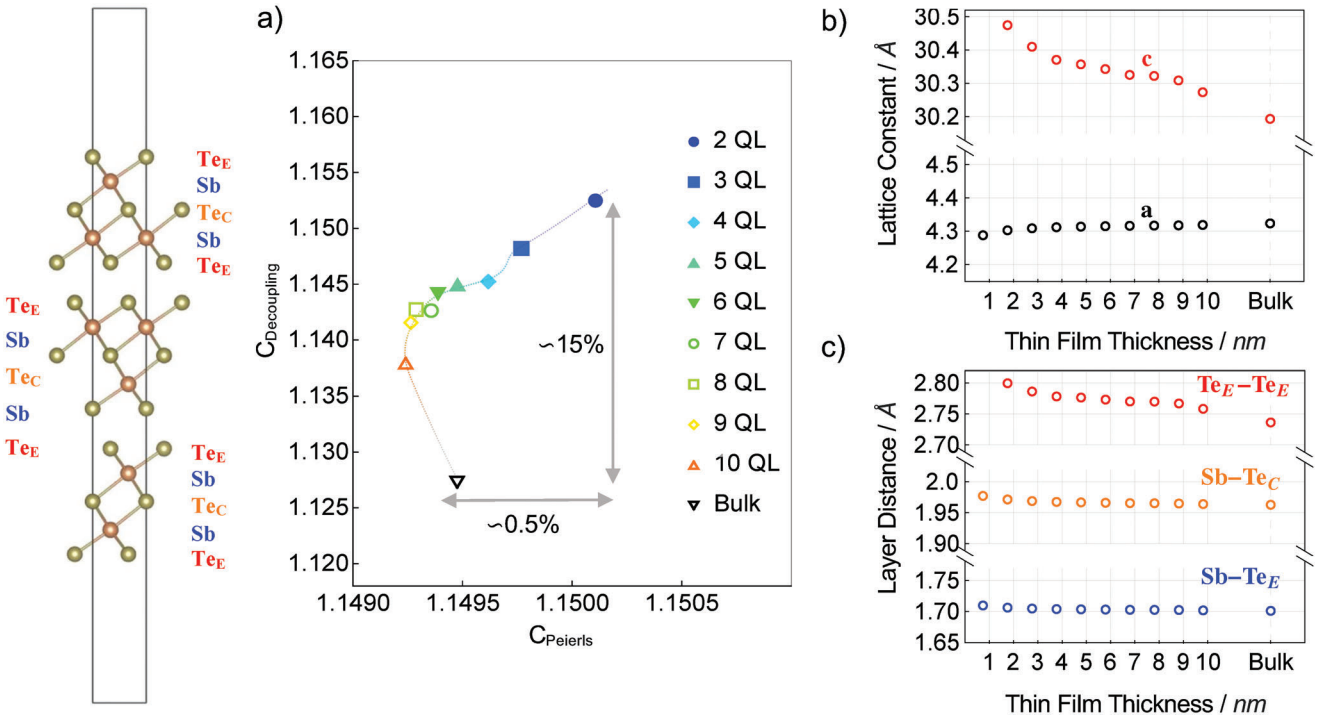

Figure 7. Thickness-dependent changes of a) decoupling and Peierls distortion coefficient, b) lattice constants, and c) atomic layer distances using the PBE+D3 approach (see Supporting Information for comparison with the PBE+D2 method). All values are averages over all similar sites in the slab. Primarily, confinement leads to quintuple decoupling, however, a slight increase in the Peierls distortion is observed as well. Thickness-dependent trends of the lattice constants are in line with XRD results. The main contribution to the increase of the *c*–axis is the Te-Te gap distance. Nevertheless, the Sb—Te_C atomic layer distance slightly increases as well.

from the model. The increase of the lattice constants with film thickness can be attributed to the increase in the Te_e–Te_e gap distance, but also within the quintuples a slightly larger distortion, given by the ratio of the two distances containing the Sb layers, can be seen.

In summary, XRD provides evidence that the confinement-induced increase in the *c*-lattice parameter mainly stems from quintuple decoupling. This is accompanied by an increase in the Te-Te gap. While hints of an in-quintuple distortion can be seen in the modeled data, potential thickness-dependent changes of the Peierls coefficient cannot be resolved experimentally, due to the limited resolution of experimental data and the numerical method employed. The following section covers the thin film structure results obtained by DFT calculations to verify the thickness trends observed and to study potential confinement-related structural distortions within the quintuples.

2.2.2. DFT Simulations of Thin Film Structure

Upon studying the atomic arrangement and chemical bonding in Sb_2Te_3 thin films with DFT, it is important to verify the adequateness of the potentials chosen. We have compared two different DFT methods (PBE+D2 and PBE+D3). The simulation results shown in the following figures are based on the PBE+D3 method because it reproduces the experimental *c*–axis value best. Nevertheless, PBE+D2 yields qualitatively similar trends, as shown in the Supporting Information (see Table S2 and Figure S13, Supporting Information).

The thickness of the simulated slabs is varied by changing the number of quintuple layers (N_{QL}) from one up to ten. Each QL consists of five atomic planes (cf. **Figure 7**). Figure 7 summarizes the most important structural properties of Sb_2Te_3 slabs as a function of film thickness after relaxation. In general, the observed trends in the atomic arrangement depend on the atomic layer position (layer index) along the (111)-direction, with surface layers being more distorted compared to layers in the middle of the slab. However, in compliance with the experimental results from coherent phonon and XRD analysis, structural trends discussed in this section are obtained from averaging over similar atomic sites within the simulated stack. A detailed discussion distinguishing center- and surface-quintuples will follow in the next section. The structural trends observed with varying film thickness are in-line with the experimental results: as the slab thickness decreases, quintuples decouple which causes the out-of-plane lattice constant (*c*) to increase. Furthermore, a slight increase in the Peierls distortion coefficient can be found, which is, compared to the increase of the decoupling coefficient, an order of magnitude smaller. Additionally, a slight decrease in the in-plane lattice constant (*a*) can be observed as well. The increase of the out-of-plane lattice constant (*c*) is mainly caused by an increase in the inter-quintuple gap. The other plane distances are changing to a lesser extent, with $\Delta(Sb - Te_E)$ being the most rigid and least changing distance.

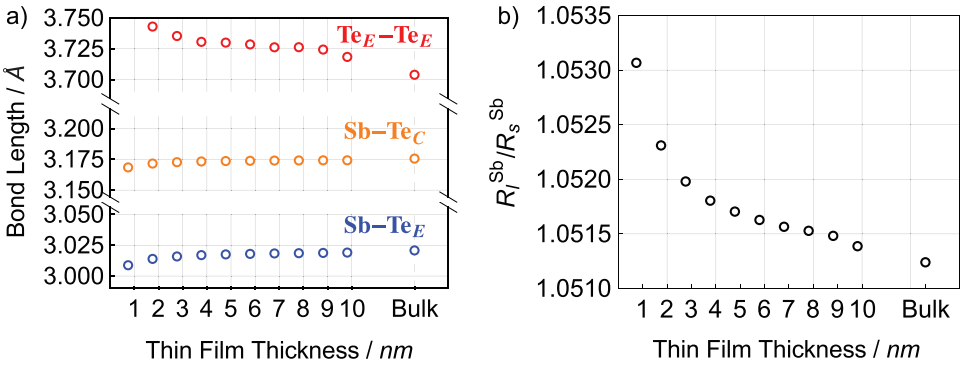

Figure 8. a) Thickness-dependent atomic bond lengths for the three different bond-types and b) long-bond to short-bond ratio between Sb and Te atoms within a quintuple.

Compared to experimental data, DFT calculations suggest an increase in the *c*-lattice parameter which is smaller by a factor of three. Therefore, changes in the distortion coefficients are slightly smaller, too.

The significance of the increase of the Te-Te gap spacing has been emphasized so far, based on XRD and DFT results for few QLs of Sb_2Te_3. On the contrary, the role of intra-quintuple distortions in the atomic arrangement has not yet been discussed. As shown in Figure 7a, a slight increase in the Peierls distortion coefficient for decreasing film thickness can be observed. As the DFT-relaxed structures contain 3D information on the thin film atomic arrangement, it is worthwhile to check if the corresponding long-bond to short-bond ratio of Sb increases as well. **Figure 8**a shows the three different bond lengths as a function of film thickness. Both, Sb—Te_c long-bond length and Sb—Te_E short-bond length shorten for the ultrathin films, with a stronger effect on the Sb—Te_E short-bond. The apparent discrepancy between plane distances and bond lengths can be explained by the accompanied in-plane compression. Contrary, the bond length across the Te-Te gap shown in Figure 8a increases for thinner films with a higher magnitude compared to the intra-quintuple changes. Figure 8b shows the long-bond to short-bond ratio of the local octahedral environment around the Sb atoms which slightly increases by 1 ‰ upon reducing the film thickness from 10 to 1 nm. This is an interesting finding: Even though both Sb bond lengths decrease, the long-bond to short-bond ratio behaves like the Peierls coefficient defined in Figure 5a. Thus, a definition of the Peierls distortion based on the Sb bond lengths yields the same trends compared to the definition based on layer distances used above.

To conclude this section, DFT simulations on the atomic arrangement of few-quintuple Sb_2Te_3 films unraveled a confinement-induced increase in the lattice constant (*c*) which arises from an inter-QL decoupling that goes along with an increased Peierls distortion. Presumably, these results are caused by a weakening of the Te—Te bonds in between the quintuples and a strengthening of the shorter bonds within the quintuples. To further evaluate this hypothesis, the next section focuses on the relation between structural confinement effects and corresponding trends for chemical bonding and their potential impact on thin film properties.

2.3. Thickness-Dependent Thin-Film Properties

To understand the changes in atomic arrangement observed in Sb_2Te_3 thin films, a quantum chemical bonding analysis is performed. Extending the quantum theory of atoms in molecules to crystalline solids, different chemical compounds have been classified by two real numbers used as bonding descriptors.[1] To derive both quantities, the crystalline solid is subdivided into nonoverlapping domains. By integrating the electron density over such a domain, the so-called domain population is obtained. Normalizing the domain population by the atomic number yields a measure for the number of electrons transferred (ET) between two adjacent atoms. Complementary, the second bonding descriptor stems from the delocalization index providing a measure for the electron sharing (ES) between adjacent atoms. As summarized in the review, changes in the Peierls-like distortion as discussed above, mainly affect the ES value.[2] Thus, the ES between adjacent atoms is considered to characterize bonding (further details provided in the review).[2] In Sb_2Te_3, there are three pairs of adjacent atoms: Sb—Te_C, Sb—Te_E, and Te_E—Te_E. Thus, three values of ES have been evaluated. In addition, DFT calculations have been carried out to investigate the thickness-dependence of the Born effective charge Z^*, a measure for the chemical bond polarizability. High values of Z^* are characteristic of compounds with a large electron-phonon coupling, thus, studying Z^* in Sb_2Te_3 thin films is interesting with respect to the coherent phonons observed over a wide thickness range. The thickness dependence of ES and Z^* will be compared to trends in the atomic arrangement quantified by the distortion motifs introduced in Section 2.2.1. The confinement-induced changes of each quantity, that is, C_{Peierls}, $C_{\text{Decoupling}}$, ES and Z^* are investigated with respect to three different averaging methods: The average over the whole slab, the average of QLs close to the surface, and close to the center, respectively.

Figure 9a,b shows the thickness-dependence of the structural distortion coefficients. A pronounced increase in the decoupling coefficient in the slab models is visible in comparison to the bulk. The two quintuple models can be described with a value of about 1.15, and larger models are slowly converging toward the bulk value of 1.125. Changes in the decoupling coefficient are found to occur homogeneously, no distinct deviations between center and surface QLs can be observed. Contrary, considering the Peierls

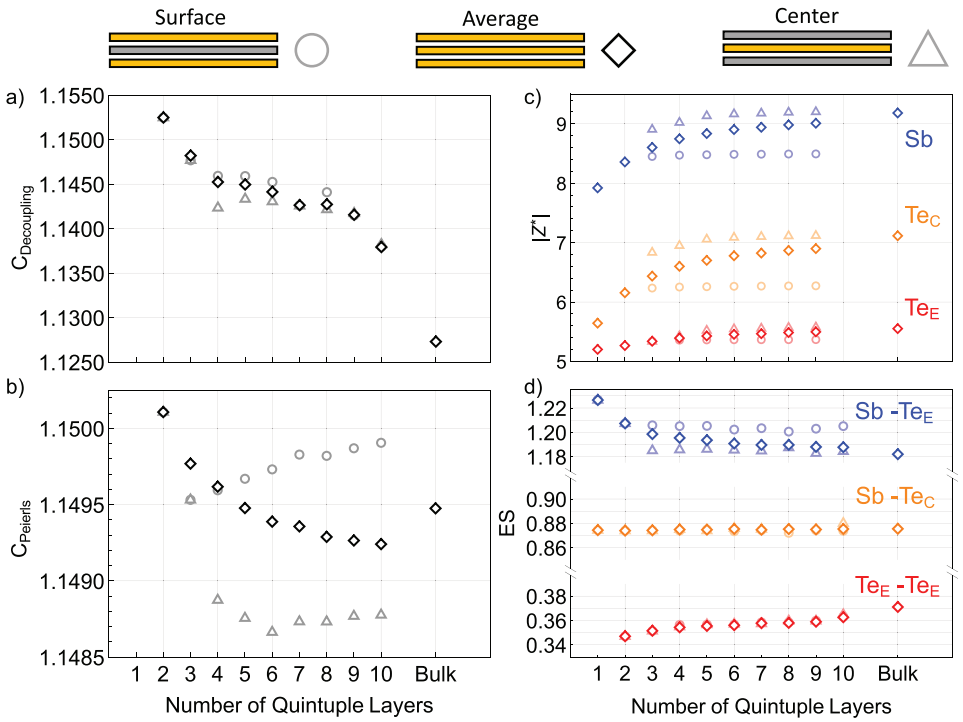

Figure 9. DFT results for the thickness-dependence of structural (left) and bonding-related properties (right) of Sb_2Te_3 thin films considering the surface (circles) and center (triangle) quintuples and the overall average (diamonds). The respective quantities are plotted as a function of film thickness expressed by the number of QLs. a,b) Structural distortion coefficients behave differently considering surface and center QLs. While QL decoupling occurs homogeneously throughout the thin films, the Peierls-coefficient is larger at the film surface compared to the center for films containing more than four QLs. c) The absolute value of the in-plane component of the Born effective charge (Z^*) increases monotonously with increasing film thickness at each atomic site. d) Electrons shared (ES) values of the three different bond types in Sb_2Te_3. Electron sharing across the Te-Te gap homogenously increases with increasing number of QLs (red) while electron sharing between Sb and the central Te merely depends on thickness. The average ES-value of the Sb—Te short-bond decreases with increasing film thickness while larger ES-values are observed at the slab surface.

distortion, differences between surface and center QLs are found in the same order of magnitude as the average changes of the coefficient. While the average value of $C_{Peierls}$ increases for thinner films, the corresponding surface values are slightly decreasing. The respective center value, which is generally below the surface value by about 0.001 is only increasing below 6 QLs. Considering the difference of $C_{Peierls}$ between bulk and surface, it is obvious that changes in the Peierls distortion arise inhomogenously throughout the Sb_2Te_3 thin film. This is presumably indicative of surface reconstruction effects. To determine whether the distortion of the buried atomic layers has an effect on surface measurements, simulated STM images of the different layer slabs have been generated and shown in Figure S14, Supporting Information. All images recover the pristine 1 × 1 Te surface, which is also observed in STM measurements of Sb_2Te_3.[3] Yet, the surface charge density of the thinnest film STM simulations (Figure S15, Supporting Information) is slightly increased compared to the 9 quintuple slab model.

Confinement-induced trends of the absolute value of the in-plane component of the Born effective charge $|Z^*_{xy}|$, which is a typical fingerprint of metavalently bonded systems if the value is much larger than the formal charge, are plotted in Figure 9. For each atomic site, $|Z^*_{xy}|$, is decreased by about 10% for the 1 quintuple model and converges toward the bulk value with increasing film thickness. with the most pronounced increase found in Sb and Te-center atoms. Te-edge atoms are least affected by slab thickness. For each atomic site, center values exceed the surface values, with the differences again being least pronounced for Te-edge.

Finally, Figure 9d shows the ES values for each bond type. Although the value is decreased for the ultrathin films compared to the bulk, it is still much larger than 0. The significant sharing of electrons across this gap is indicative of a pronounced interaction between quintuples. This finding supports the view that the bonding across the gap is stronger than in purely vdW-bonded systems. A homogeneous and continuous increase of the ES value of the Te-Te gap with increasing film thickness is found, indicating a stronger QL interaction across the gap in the thicker films. Consequently, changes in the localization of electrons between QLs cannot be considered as an interface effect but emerge as an inherent confinement effect of metavalent solids. Regarding the Sb—Te long-bond, no significant thickness-dependent changes can be

observed very different from the corresponding short-bond, whose ES value markedly decreases when films get thicker. Interestingly, those changes differ between slab center and surface: surface ES values are larger compared to the center ones, as the distortion is increased.

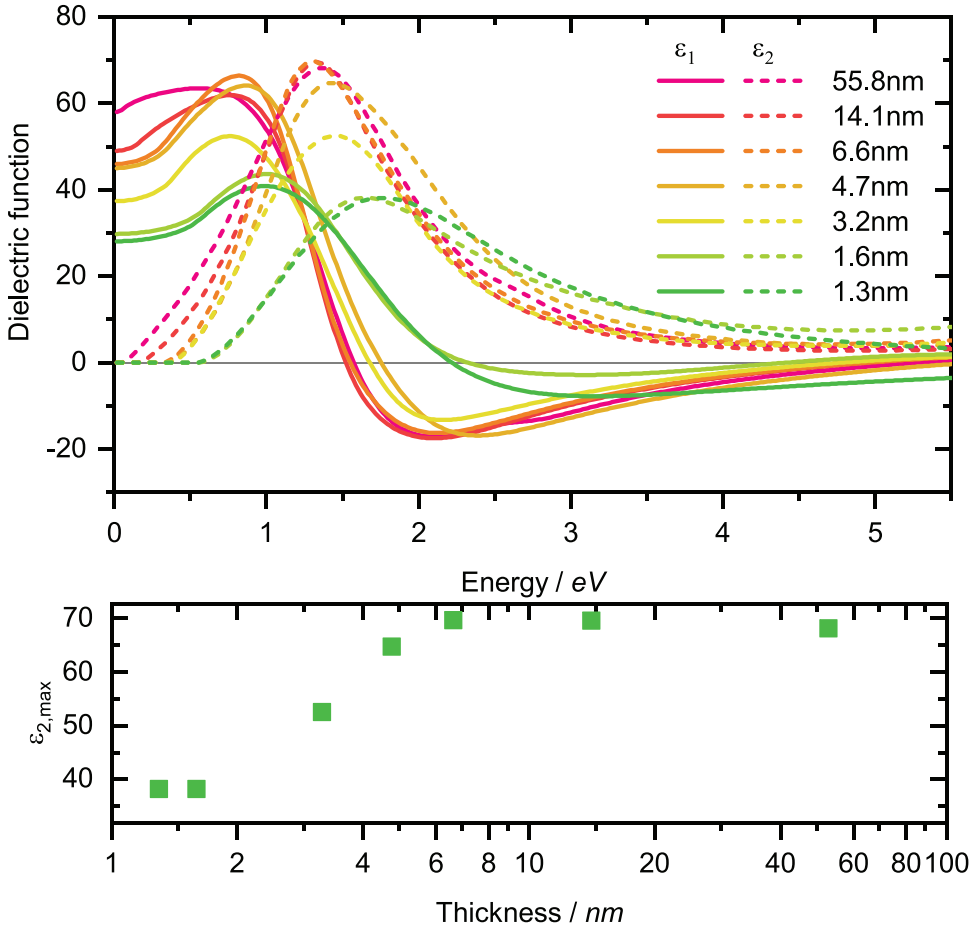

Figure 10. The dielectric function of various Sb_2Te_3 thin films obtained from spectroscopic ellipsometry. To focus on optical transitions in the visible spectrum, the Drude contribution is excluded in the plot. A distinct reduction of $\epsilon_{2,max}$ is observed in ultrathin films.

2.4. Investigation of the Optical Response to the Confinement Effect

The preceding sections shed light on the subtle interplay between bonding and thin-films structural distortions in thin Sb_2Te_3 films. Ultrathin films exhibit more pronounced structural distortions compared to thicker films in turn resulting in a higher ES-value at the quintuple interfaces and a lower value of electrons shared in between the quintuples. In previous work, it is claimed that the dielectric function of metavalently bonded materials is tunable by thin-film thickness.[9] There, distinct variations of bonding with film thickness have been identified to cause those property changes in metavalent materials with a rocksalt high-symmetry structure such as Sb or GeTe. A larger Peierls distortion in those materials was found to reduce the orbital overlap reducing the matrix element for the transition between available initial (occupied) and final (unoccupied) states. Thus, it is worthwhile to explore the potential to tune optical properties of confined metavalently bonded sesquichalcogenides. For this purpose, the averaged (isotropic) dielectric function of the Sb_2Te_3 films was fitted from spectroscopic ellipsometry data and is shown in **Figure 10**. In order to properly discuss the optical transitions in the visible spectrum, the Drude contribution is subtraced and only the resulting dielectric function is depicted in the plot. The maximum of ϵ_2 decreases to 40 in the thinnest films and gradually recovers to 70 in the thicker films. A similar trend was also reported for thin films of Bi_2Se_3.[29] The DFT-based orbital resolved dielectric function is an efficient tool to link the observed structural distortions to variations in the absorption quantified by the maximum of ϵ_2. The orbital resolved dielectric function of bulk Sb_2Te_3 is calculated and shown in **Figure 11**. Similar to the situation in monochalcogenides, the optical response of bulk Sb_2Te_3 in the visible region is governed by p–p transitions.

The bonding analysis in the previous part shed light on the significant bonding contribution across the quintuple gaps. Thus, optical transitions based on gap-crossing orbitals exist, if occupied and unoccupied states are available in the bands corresponding to those orbitals. Figure 11b shows the orbital projection from the DOS calculated for the 5-QL slab model. The projection of Te-orbitals is split between central and edge Te sites. The contributions of the first maxima in the DOS below and above EF are the initial and final states of the maximum in the optical transition, respectively. The major contribution to the unoccupied states stems from Sb-p orbitals and the Te edge p-orbitals. In contrast, the occupied states are governed by the Te p-orbitals from all sites, with a small contribution from the Sb s-orbitals. Thus,

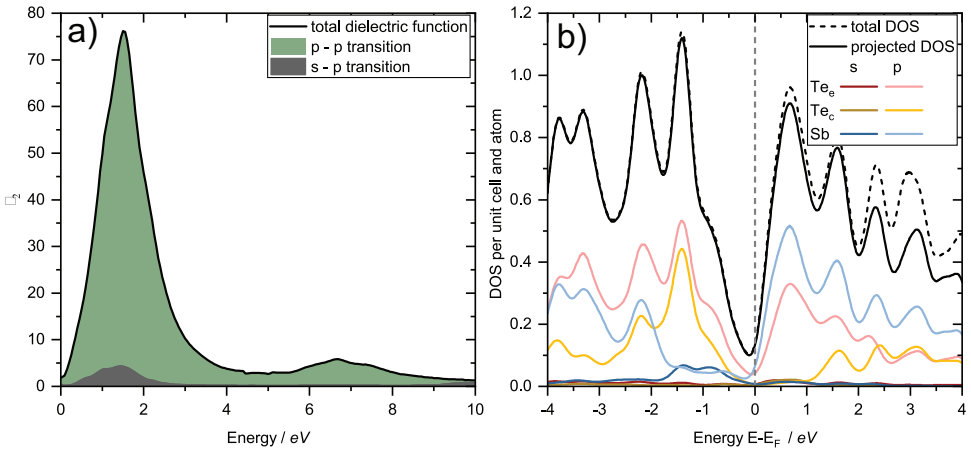

Figure 11. a) Orbital resolved dielectric function and b) calculated projected density of states of bulk Sb_2Te_3 obtained by DFT simulation. The data is averaged over all directions to facilitate the comparison with experimental data. The optical response is governed by p–p transitions. For the central Te atom, transitions to adjacent Sb atoms are available. For the edge Te atoms, transitions are available both to the Sb atoms and to Te atoms on the other side of the gap.

optical transitions involved in the maximum of the dielectric function are indeed transitions from Te p-like states from all sites to the Sb p-like states and transitions from Tep-like states at the edges to Te p-like states from the neighboring Te at the gaps.

Consequently, orbital overlap reduction across the gap and within each QL reduces the transition rate due to Fermis golden rule and in turn the materials' optical absorption. Orbital overlap across the gap can be tuned by the quintuple decoupling while intra-quintuple overlap is tunable via Peierls-distortion.

However, as evident from Figure 10, even in ultrathin films, the thin film's absorption is quite pronounced ($\epsilon_{2\max} \approx 40$). Due to the inversion symmetry of the quintuples, the bond angle of the Sb-Te_c-Sb trimer is fixed at 180°, and the overlap is less affected by distortions, which could explain the relatively high residual value of $\epsilon_{2\max}$ observed in the ultrathin films.

3. Discussion

In the last section, distinct thickness-dependent trends of structural and physical properties in Sb_2Te_3 thin films have been identified and compared to changes in the chemical bonding. Similar to a recent study about pronounced confinement effects of the metavalently bonded monochalcogenide GeTe, the observed scaling effects in crystalline Sb_2Te_3 thin films can be linked to the peculiar position of MVB materials in the bonding map between metallic and covalent systems.[9,30] In this region of the map, chemical bonding is characterized by a competition of electron localization and delocalization which can be strongly affected by material confinement. However, due to its structural anisotropy, Sb_2Te_3 behaves quite differently from GeTe if present in reduced dimensions. In rhombohedral GeTe, where only one bond-type needs to be considered, confinement leads to an increased ES between adjacent atoms inducing an increased Peierls distortion and distinct changes in structural, vibrational, and optical properties. In contrast, as three different bond-types have to be distinguished in Sb_2Te_3, relating thickness-dependent trends of chemical bonding to structural and physical properties needs further distinction. Therefore, to identify correlations between chemical bonding, structural distortions and physical properties of Sb_2Te_3 thin films, surface, center, and average values have to be distinguished as shown in Figure 9.

Following this argument, two correlations between the chemical bonding descriptor ES and the structural distortion coefficients can be identified. The first correlation concerns the ES value of adjacent Te edge atoms on the one hand and the decoupling coefficient on the other hand: thickness-dependent trends of both quantities occur throughout the thin film (see Figure 9a,d) indicating that QL decoupling in ultrathin films is induced by less ES between Te edge sites.

In contrast, thickness-dependent trends of ES between adjacent Sb and Te edge atoms as well as the Peierls distortion arise inhomogenously as can be seen in Figure 9b,d. This correlation is reasonable as an increased Peierls distortion by definition leads to decreased Sb—Te_E atomic plane spacings as can be seen from Figure 5b, indicating a more rigid bonding between these atoms. Generally, metavalently bonded systems suffer a larger Peierls distortion when pushed toward more covalent character, for example, reaching larger ES values either via stoichiometry variations or by confinement.[2] Consequently, surface QLs with a more pronounced Peierls distortion show larger ES values (ES > 1.2) compared to the center QLs (ES < 1.19).

Large values of the Born effective charge $|Z^*|$ are indicative of a pronounced chemical bond polarizability and have been identified as a typical fingerprint of metavalently bonded materials. On the contrary, covalent systems, characterized by larger Peierls distortions and larger ES-values, typically possess smaller Born effective charges.[10] Considering the average values throughout the whole films, the reduction of the Peierls distortion correlates with the increase of the Born effective charge as expected for thicker films. This change is accompanied by smaller intra-quintuple ES-values. Furthermore, for each atomic site, $|Z^*|$ values are larger, and confinement-induced dropping of $|Z^*|$ is most pronounced for the quintuples at the center of the slab which fits the observations found for the Peierls distortion. These findings demonstrate the strong correlation between the Peierls distortion and corresponding thin film properties.

In crystalline GeTe thin films, Raman measurements have demonstrated a distinct increase of the A1-mode frequency with decreasing film thickness which has been linked to a confinement-induced phonon stiffening caused by the stronger Peierls distortion found in ultrathin GeTe films.[9] Contrary to those observations, the coherent phonon frequency of the out-of-plane $A_{1g}{}^1$-mode in Sb_2Te_3 thin films decreases with decreasing film thickness. Interestingly, similar observations have been made for nanoplatelets of the metavalently bonded compound Bi_2Se_3 and attributed to weaker effective restoring forces across the van-der-Waals like gap in ultrathin samples.[8] Along this line of reasoning, we attribute the confinement-induced coherent phonon ($A_{1g}{}^1$ symmetry) softening found here to the pronounced quintuple decoupling causing the effective restoring force on the outer Te and Sb atoms to decrease. In contrast to the $A_{1g}{}^1$ phonon mode, the $A_{1g}{}^2$ mode frequency markedly increases in ultrathin films with decreasing thickness. Out of the three different bond lengths in Sb_2Te_3, the Sb—Te_E intra-quintuple bond length is most strongly affected by atomic displacements of $A_{1g}{}^2$ symmetry. Contrary to the decoupling motif which quantifies the interaction between two quintuples, the Peierls motif describes changes in the bond lengths within the quintuple. Consequently, the stiffening of the $A_{1g}{}^2$ symmetric phonon mode observed in thinner films can be attributed to the corresponding increase of the Peierls distortion.

The direct observations of thickness-dependent distortions of Sb_2Te_3 thin films are also intriguing concerning properties of topologically non-trivial states. As topological surface states of Sb_2Te_3 (TI) are protected by spatial inversion symmetry, a phase transition between normal insulator and TI is expected, which is consistent with the collapse of topological surface states at ultrathin films (<5 nm).[31] In conjunction with our precedent study on ultrathin GeTe, exotic properties of GeTe/Sb_2Te_3 superlattice are expected to be clarified such as spin battery and superior memory performances.[32,33] Notably, this performance improvement critically depends on the thickness of the sublayers and is experimentally optimized, but underlying mechanisms are not yet discussed. [GeTe 0.8 nm/Sb_2Te_3 1 nm] films are best for the spin battery while [GeTe 0.8 nm/Sb_2Te_3 4 nm] films are most suited for memory application. Bonding properties depending on the thicknesses of sublayers in the competition between covalency and metavalency apparently shed light on the underlying mechanisms of optimized thicknesses of sublayers.

Furthermore, due to their non-volatile multilevel switching-ability, phase-change memories have been revisited recently to realize in-memory computing hardware based on integrated photonic cells.[34] Based on their high-bandwidth, wavelength division multiplexing ability, and vanishing amorphous drift, integrated photonic phase-change memory cells yield attractive properties potentially surpassing the performance of electric phase-change memory devices. However, considering energy-consumption, integrated photonic phase-change cells lack efficiency due to the limited scaling ability of SiN waveguides.[35] Switching from SiN to AlN waveguides with improved scaling abilities brings along the necessity to identify phase-change materials with low losses and high optical contrast in the visible spectral range. This turns out to be challenging as phase-change materials are typically used in the infrared due to their low optical bandgap. Generally, substituting the anion-site in tellurium-based PCMs with lighter chalcogens increases the bandgap. Consequently, the covalent systems Sb_2S_3 and Sb_2Se_3 have been proposed for photonic applications in the visible spectral range. However, as the moderate optical contrast in those systems does not stem from a change of the bonding mechanism but from the huge density contrast between amorphous and crystalline state, using Sb_2S_3 and Sb_2Se_3 potentially limits the cells cycling endurance and signal-to-noise ratio.[36] To avoid these limitations, pronounced confinement-related changes in the bandgap energy in colloidal GeTe nanoparticles have been exploited to tune the optical properties for photonic applications of GeTe in the visible spectral range.[37] Recent studies on monatomic phase-change memories highlight the confinement-related tuneability of crystallization kinetics of elemental antimony and its relevance for electrically switching phase-change memory cells.[38,39] The distinct correlation between optical properties and film thickness discussed in the previous section emphasizes the confinement-related tuning abilities of Sb_2Te_3 and potentially triggers further investigations with respect to the applicability of Sb_2Te_3 nanoparticles for integrated photonic devices working in the visible spectral range. To that end, further studies on the thickness-dependency of crystallization kinetics and the stability of the amorphous phase at room temperature are desirable.

4. Conclusion

Pronounced THz-rate oscillations in the transient reflectivity signal of few-nanometer crystalline Sb_2Te_3 thin films were found and identified as DECP of $A_{1g}{}^1$-symmetry. A distinct drop in coherent phonon frequency for ultrathin films has been observed and linked to a quintuple-decoupling as identified by XRD analysis. DFT simulations on the thin film structure revealed an increased Peierls distortion for decreasing film thickness which was found to be closely related to the thickness dependence of thin film properties. The observed confinement-induced vibrational, structural, and property-related changes have been discussed in terms of a novel bonding mechanism that has been recently introduced to explain the extraordinary properties of many chalcogenide-based functional materials with applications ranging from phase-change memories to thermoelectric devices. The distinct confinement effects observed in Sb_2Te_3, and emerging tuning abilities have been linked to the optimization of interfacial phase-change memories, TI-devices, and photonic applications.

5. Experimental Section

Sample Preparation: Sb_2Te_3 thin films studied in this work were prepared by MBE on a high quality 35 mm × 35 mm Si (111) substrate (N/Ph doped, 3–10 kΩ cm resistivity). Prior to substrate insertion in deposition chamber, the substrates were cleaned through standard RCA cleaning process followed by oxide removal via submersion in 1% hydrogen fluoride solution. In the last step, the substrates were rinsed in deionized water and dried using nitrogen gas. This creates a weak H-passivated layer on top of Si that enables suitable transfer from wet bench to the deposition chamber. Before deposition of Sb_2Te_3, the surface of Si was reconstructed to Sb termination (Si(111)-($\sqrt{3} \times \sqrt{3}$) R30°- Sb), which was evidenced by the recognizable RHEED pattern. Sb termination was chosen to have the least number of rotational domains and bigger grain size to disregard the possible artifacts due to grain boundaries. Deposition was performed

at ultra-high vacuum conditions (base pressure ≈ 10^{-10}–10^{-11} mbar) on the substrate maintained at 150 °C. Sb_2Te_3 was grown under Te rich conditions with flux ratio of Sb:Te = 2:5 which provides growth rate of 15 nm h^{-1}. Growth was monitored using Reflection High Energy Electron Diffraction (RHEED) imaging and the variation of in-plane constant with thickness was calculated post deposition.

After the deposition, Sb_2Te_3 films were transferred to the oxide deposition chamber (without breaking the vacuum) where Al_2O_3 was deposited on top using electron-beam evaporation. Substrate was rotated at 6 rpm to deposit the oxide layer homogeneously. Al_2O_3 was deposited to avoid surface oxidation upon transfer of samples from MBE to other analysis tools.

Femtosecond Pump-Probe Reflectivity Measurements: Ultrafast optical measurements were performed using a common reflection type, two color pump-probe experiment in isotropic and anisotropic (electro-optic sampling) scheme. The pump-beam of 800 nm wavelength and 90 fs width was decoupled from a Ti:Sapphire regenerative femtosecond amplifier, harmonically chopped at 375 Hz, and guided to an optical delay line before it was focused on the sample to a spot-size of 60 µm diameter. The probe pulses were frequency converted to 520 nm (isotropic scheme) and 635 nm (anisotropic scheme) by an optical parametric amplifier and focused to a 30 µm spot on the sample. In isotropic sampling, the detection unit includes two balanced Si-photodiodes connected to variable gain current amplifiers, and a data-acquisition card; the signal detection scheme is adapted from ref. [40]. All measurements were performed at the same pump fluency at the order of 1 mJ cm^{-2} while the probe fluency was smaller by a factor of 10. To avoid long-term sample modification during measurement, a fresh sample spot was adjusted for each delay position. Unphysical correlations between sample spot position and delay setting were prevented by a random walk. Furthermore, the anisotropic transient reflectance was calculated from the s- and p-polarized components of the reflected light using the electro-optic detection scheme.[22]

$$\Delta R_{EO} = \frac{\Delta\left(R_s - R_p\right)}{R_0} \tag{5}$$

A polarizing beamsplitter cube was used to split the reflected probe beam correspondingly. Anisotropic measurements were performed at a probe-wavelength of 635 nm. In the EO-scheme, the pump-fluency was reduced such that measurements could be performed on a single spot for optimized signal-to-noise ratio. Both, isotropic and anisotropic transient reflectance was normalized to the steady state reflectance R_0. Reversibility of optical excitation was ensured by monitoring the static reflectivity gained by the probe signals when the pump-pulse was chopped. Additionally, light microscope images were taken to identify potential sample modifications; no such indications could be found.

Raman Spectroscopy Measurements: The Raman spectroscopy measurements were acquired in backscattering geometry and conducted at room temperature, using a commercial WITec system (alpha300). A laser with a wavelength of 532 nm (2.33 eV) was used for excitation, which was delivered through a single-mode optical fiber. By employing a long working focusing lens with a numerical aperture of 0.80, the spot size of ≈400–500 nm was obtained. The excitation power was set to 500 µW, to avoid heating effects. For detection, a single-mode optical fiber and a charge-coupled spectrometer with a grating of 2400 lines mm^{-1} were used. All measurements were performed with linear laser polarization and a 50× (NA = 0.7) objective.

X-Ray Reflection/Diffraction Measurements: For the XRR measurements and theta-2-theta measurements, a Bruker D8 Discover with a Cu $K_{\alpha,1}$ radiation source (1.5406 Å) was used. Theta 2 theta measurements were done with a Goebel mirror, a 0.6 mm slit, a (220) Ge monochromator, an automatic rotary absorber on the incident beam, and a LynxEye detector in the 0-D mode with an active area of 0.675 mm on the detector side.

The thickness of the thin films was obtained from XRR measurements which were performed with 0.1 mm slits instead. The reciprocal space maps were taken on a Rigaku SmartLab X-Ray Diffractometer equipped with a HyPix-3000 2D detector which was preset to the 1D-mode. A Ge(220) × 2 monochromator was used for the incident beam and a 5.0° Soller slit for the outgoing beam. To obtain peak positions, the curves were fitted with Pseudo-Voigt profiles. The lattice parameters were determined by means of a linear regression. The XRR measurements were analyzed with a 2-layer model in GenX (see Figure S3 and Table S1, Supporting Information).

The kinematical diffraction simulations were performed with the SimStack class in MATLAB [https://zenodo.org/badge/DOI/10.5281/zenodo.4386528.svg], generating 50 individual atomic stacks and the diffraction pattern I(Qz) for each stack. The resulting incoherent superposition was multiplied by a geometric function $I \propto N_{scatterer} \propto \sin\theta^2$ to account for the changing sample illumination during the measurement.

For the integration of the diffracted intensities, the measurements were plotted in reciprocal space and a region of interest (ROI) was defined around the peaks. The background within the ROI was estimated by averaging the background intensity on both sides of the ROI. Error Bars on the Integrated Volume arise from calculating the background intensity from a weighted average with the weights 1/4 and 3/4 and vice versa. The ROI and the area for background calculation were kept constant across all samples. Error bars on the further data were propagated from evaluation of the lower/upper values of the integrated volume.

DFT Studies: All calculations on thin films were performed using the plane wave code pw.x included in the Quantum Espresso package.[41] Scalar relativistic projector-augmented-wave pseudopotentials were used. The PBE form of the generalized gradient approximation was employed.[42] Since PBE cannot properly describe the weak vdW type interactions in layered materials, two semiempirical vdW corrections (D2 and D3) were included to improve the description.[43] A vacuum region of thickness ≈20 Å was added to decouple the periodic images of the slabs. As regards the sampling of the Brillouin zone, an 8 × 8 × 1 mesh was used for all the thin-film models. For phonon calculations, density functional perturbation theory was used as implemented in the ph.x code of the Quantum Espresso package. In this code, phonon calculations for the PBE-D3 functional are not yet implemented. Thus, PBE-D2 was used to compute the frequencies shown in Figure 2c. Additionally, STM simulations have been conducted using the post-processing step of Quantum Espresso. Visualization of STM simulations was done using the open-source software VESTA. Structural relaxation was performed on a 12 × 12 × 1 hexagonal slab supercell model. The following calculation parameters were used: convergence threshold on total energy for ionic minimization: 1.0 e-5 (a.u.), convergence threshold on forces for ionic minimization: 1.0e-4, convergence threshold on the pressure for variable cell relaxation: 0.5 kbar, kinetic energy cutoff for wavefunctions: 50 Ry, kinetic energy cutoff for charge density: 500 Ry, convergence threshold for self-consistency: 1.0e-12.

Electron share values were quantified as two times the corresponding bond order, which was calculated using the density-derived electrostatic and chemical (DDEC6) approach.[44]

The electronic structure calculations were conducted using DFT, utilizing optimized norm-conserving Vanderbilt pseudo potentials as implemented in the Quantum Espresso software packages.[41,45] GGA-PBE exchange-correlation functionals were used for the computation.[42] The energy cutoffs exceeded 100 Ry for all calculations. An 18 × 18 × 18 k-point grid was utilized for the calculation of the band structure. More Information about the DFT structures, including a comparison to experimental values of Bulk Sb_2Te_3[46] can be found in the Supporting Information

Dielectric Function Data: Ellipsometry spectra were measured on a J.A.Woollam M-2000UI spectroscopic ellipsometer. The deuterium and halogen lamps served as the sources of illumination for the setup. A silicon CCD camera detected visible and ultraviolet light, while an InGaAs diode array captured lower energy photons. In total, 584 channels with an average of 7 meV resolution over 0.72 to 5.14 eV were available. The reflectance data were collected by FTIR and fiber grating over 1000 to 40 000 cm^{-1} range (Vertex 80v, Bruker). Dielectric functions of samples were derived using a three-layer model (capping/thin film/substrate) through matrix formalism in the CODE software. The dielectric function of the Sb_2Te_3 thin films was described by employing a summation of a constant dielectric background along with Tauc-Lorentz oscillators and Drude contributions,

similar to the data processing in previous studies.[9] The contributions of ellipsometry spectra and reflectance spectra to the fitted dielectric function were weighted by a factor to make them contribute equally to the mean squared deviation. A Downhill simplex method was employed for the unconstrained optimization. All the parameters were fitted to convergence.

Atomic Force Microscopy: Atomic force microscopy measurements shown in the supplement were taken by a Nanoscope Dimension 3000 and were analyzed using Gwyddion. The scan lines shown in the images were aligned with the "matching" algorithm. Roughnesses were calculated from 5×5 micron images, while 2×2 micron are shown in Figure S5, Supporting Information to highlight different morphologies.

Supporting Information

Supporting Information is available from the Wiley Online Library or from the author.

Acknowledgements

J.M. and P.K. contributed equally to this work. The authors gratefully acknowledge the computational resources by the JARA-HPC from RWTH Aachen University under project JARA0236 and the computing time provided to them at the NHR Center NHR4CES at RWTH Aachen University (project number p0020357). This work was supported in part by the Deutsche Forschungsgemeinschaft (SFB 917) and in part by the Federal Ministry of Education and Research (BMBF, Germany) in the project NEUROTEC II (16ME0398K). The authors thank Sophia Wahl for conducting the reflectance measurements using FTIR.

Open access funding enabled and organized by Projekt DEAL.

Conflict of Interest

The authors declare no conflict of interest.

Data Availability Statement

The data that support the findings of this study are available from the corresponding author upon reasonable request.

Keywords

coherent phonons, confinement, metavalent bonding, sesquichalcogenides, topological Insulators

Received: July 5, 2023
Revised: August 28, 2023
Published online: September 19, 2023

[1] J.-Y. Raty, M. Schumacher, P. Golub, V. L. Deringer, C. Gatti, M. Wuttig, *Adv. Mater.* **2019**, *31*, 1806280.
[2] B. J. Kooi, M. Wuttig, *Adv. Mater.* **2020**, *32*, 1908302.
[3] G. Wang, X. Zhu, J. Wen, X. i. Chen, K. e. He, L. Wang, X. Ma, Y. Liu, X. i. Dai, Z. Fang, J. Jia, Q. Xue, *Nano Res.* **2010**, *3*, 874.
[4] Y.-Y. Li, G. Wang, X.-G. Zhu, M.-H. Liu, C. Ye, X. i. Chen, Y.-Y. Wang, K. He, L.-L. Wang, X.-C. Ma, H.-J. Zhang, X. i. Dai, Z. Fang, X.-C. Xie, Y. Liu, X.-L. Qi, J.-F. Jia, S.-C. Zhang, Q.-K. Xue, *Adv. Mater.* **2010**, *22*, 4002.
[5] K. A. Messalea, A. Zavabeti, M. d. Mohiuddin, N. Syed, A. Jannat, P. Atkin, T. Ahmed, S. Walia, C. F. Mcconville, K. Kalantar-Zadeh, N. Mahmood, K. Khoshmanesh, T. Daeneke, *Adv. Mater. Interfaces* **2020**, *7*, 2001131.
[6] A. Bafekry, M. Faraji, M. M. Fadlallah, H. R. Jappor, N. N. Hieu, M. Ghergherehchi, S. A. H. Feghhi, D. Gogova, *J. Phys. D: Appl. Phys.* **2021**, *54*, 395103.
[7] A. Bafekry, B. Mortazavi, M. Faraji, M. Shahrokhi, A. Shafique, H. R. Jappor, C. Nguyen, M. Ghergherehchi, S. A. H. Feghhi, *Sci. Rep.* **2021**, *11*, 10366.
[8] J. Zhang, Z. Peng, A. Soni, Y. Zhao, Y. i. Xiong, B. o. Peng, J. Wang, M. S. Dresselhaus, Q. Xiong, *Nano Lett.* **2011**, *11*, 2407.
[9] P. Kerres, Y. Zhou, H. Vaishnav, M. Raghuwanshi, J. Wang, M. Häser, M. Pohlmann, Y. Cheng, C.-F. Schön, T. Jansen, C. Bellin, D. E. Bürgler, A. R. Jalil, C. Ringkamp, H. Kowalczyk, C. M. Schneider, A. Shukla, M. Wuttig, *Small* **2022**, *18*, 2201753.
[10] M. Wuttig, V. L. Deringer, X. Gonze, C. Bichara, J.-Y. Raty, *Adv. Mater.* **2018**, *30*, 1803777.
[11] R. Arora, U. V. Waghmare, C. N. R. Rao, *Adv. Mater.* **2023**, *35*, 2208724.
[12] H. Zhang, C.-X. Liu, X.-L. Qi, X. Dai, Z. Fang, S.-C. Zhang, *Nat. Phys.* **2009**, *5*, 438.
[13] R. Wang, F. R. L. Lange, S. Cecchi, M. Hanke, M. Wuttig, R. Calarco, *Adv. Funct. Mater.* **2018**, *28*, 1705901.
[14] A. Bafekry, M. Faraji, S. Karbasizadeh, I. A. Sarsari, H. R. Jappor, M. Ghergherehchi, D. Gogova, *Phys. Chem. Chem. Phys.* **2021**, *23*, 24336.
[15] A. M. Mio, P. M. Konze, A. Meledin, M. Küpers, M. Pohlmann, M. Kaminski, R. Dronskowski, J. Mayer, M. Wuttig, *Adv. Funct. Mater.* **2019**, *29*, 1902332.
[16] Y. Hao, Y. Wang, L. Wang, Z. Ni, Z. Wang, R. Wang, C. K. Koo, Z. Shen, J. T. L. Thong, *Small* **2010**, *6*, 195.
[17] Y. Wang, L. Guo, X. Xu, J. Pierce, R. Venkatasubramanian, *Phys. Rev. B* **2013**, *88*, 064307.
[18] M. Weis, K. Balin, R. Rapacz, A. Nowak, M. Lejman, J. Szade, P. Ruello, *Phys. Rev. B* **2015**, *92*, 014301.
[19] G. C. Cho, W. Kütt, H. Kurz, *Phys. Rev. Lett.* **1990**, *65*, 764.
[20] H. J. Zeiger, J. Vidal, T. K. Cheng, E. P. Ippen, G. Dresselhaus, M. S. Dresselhaus, *Phys. Rev. B: Condens. Matter Mater. Phys.* **1992**, *45*, 768.
[21] G. A. Garrett, T. F. Albrecht, J. F. Whitaker, R. Merlin, *Phys. Rev. Lett.* **1996**, *77*, 3661.
[22] T. Dekorsy, T. Pfeifer, W. Kütt, H. Kurz, *Phys. Rev. B: Condens. Matter Mater. Phys.* **1993**, *47*, 3842.
[23] K. Norimatsu, M. Hada, S. Yamamoto, T. Sasagawa, M. Kitajima, Y. Kayanuma, K. G. Nakamura, *J. Appl. Phys.* **2015**, *117*, 143102.
[24] Y. Li, V. A. Stoica, L. Endicott, G. Wang, C. Uher, R. Clarke, *Appl. Phys. Lett.* **2010**, *97*, 171908.
[25] Y. Wang, X. Xu, R. Venkatasubramanian, *Appl. Phys. Lett.* **2008**, *93*, 113114.
[26] J. E. Boschker, J. Momand, V. Bragaglia, R. Wang, K. Perumal, A. Giussani, B. J. Kooi, H. Riechert, R. Calarco, *Nano Lett.* **2014**, *14*, 3534.
[27] M. Lewin, L. Mester, T. Saltzmann, S.-J. Chong, M. Kaminski, B. Hauer, M. Pohlmann, A. M. Mio, M. Wirtssohn, P. Jost, M. Wuttig, U. Simon, T. Taubner, *ACS Appl. Nano Mater.* **2018**, *1*, 6834.
[28] Y. Liu, M. Weinert, L. Li, *Phys. Rev. Lett.* **2012**, *108*, 115501.
[29] M. Fang, Z. Wang, H. Gu, M. Tong, B. Song, X. Xie, T. Zhou, X. Chen, H. Jiang, T. Jiang, S. Liu, *Appl. Surf. Sci.* **2020**, *509*, 144822.
[30] L. Guarneri, S. Jakobs, A. Von Hoegen, S. Maier, M. Xu, M. Zhu, S. Wahl, C. Teichrib, Y. Zhou, O. Cojocaru-Mirédin, M. Raghuwanshi, C.-F. Schön, M. Drögeler, C. Stampfer, R. P. S. M. Lobo, A. Piarristeguy, A. Pradel, J.-Y. Raty, M. Wuttig, *Adv. Mater.* **2021**, *33*, 2102356.
[31] Y. Zhang, K. He, C.-Z. Chang, C.-L. Song, L.-L. Wang, X. Chen, J.-F. Jia, Z. Fang, X. Dai, W.-Y. Shan, S.-Q. Shen, Q. Niu, X.-L. Qi, S.-C. Zhang, X.-C. Ma, Q.-K. Xue, *Nat. Phys.* **2010**, *6*, 584.
[32] J. Tominaga, N. Miyata, S. Sumi, H. Awano, S. Murakami, *npj 2D Mater. Appl.* **2020**, *4*, 22.
[33] R. E. Simpson, P. Fons, A. V. Kolobov, T. Fukaya, M. Krbal, T. Yagi, J. Tominaga, *Nat. Nanotechnol.* **2011**, *6*, 501.
[34] X. Li, N. Youngblood, C. Ríos, Z. Cheng, C. D. Wright, W. Pernice, H. Bhaskaran, *Optica* **2018**, *6*, 1.

[35] M. S. Arjunan, S. Durai, A. Manivannan, *Phys. Status Solidi RRL* **2021**, *15*, 2100291.
[36] M. Wuttig, H. Bhaskaran, T. Taubner, *Nat. Photonics* **2017**, *11*, 465.
[37] A.-K. U. Michel, M. Sousa, M. Yarema, O. Yarema, V. Ovuka, N. Lassaline, V. Wood, D. J. Norris, *ACS Appl. Nano Mater.* **2020**, *3*, 4314.
[38] M. Salinga, B. Kersting, I. Ronneberger, V. P. Jonnalagadda, X. T. Vu, M. Le Gallo, I. Giannopoulos, O. Cojocaru-Mirédin, R. Mazzarello, A. Sebastian, *Nat. Mater.* **2018**, *17*, 681.
[39] D. T. Yimam, B. J. Kooi, *ACS Appl. Mater. Interfaces* **2022**, *14*, 13593.
[40] C. A. Werley, S. M. Teo, K. A. Nelson, *Rev. Sci. Instrum.* **2011**, *82*, 123108.
[41] P. Giannozzi, S. Baroni, N. Bonini, M. Calandra, R. Car, C. Cavazzoni, D. Ceresoli, G. L. Chiarotti, M. Cococcioni, I. Dabo, A. Dal Corso, S. De Gironcoli, S. Fabris, G. Fratesi, R. Gebauer, U. Gerstmann, C. Gougoussis, A. Kokalj, M. Lazzeri, L. Martin-Samos, N. Marzari, F. Mauri, R. Mazzarello, S. Paolini, A. Pasquarello, L. Paulatto, C. Sbraccia, S. Scandolo, G. Sclauzero, A. P. Seitsonen, et al., *J. Phys.: Condens. Matter* **2009**, *21*, 395502.
[42] J. P. Perdew, K. Burke, M. Ernzerhof, *Phys. Rev. Lett.* **1996**, *77*, 3865.
[43] S. Grimme, J. Antony, S. Ehrlich, H. Krieg, *J. Chem. Phys.* **2010**, *132*, 154104.
[44] T. A. Manz, *RSC Adv.* **2017**, *7*, 45552.
[45] D. R. Hamann, *Phys. Rev. B* **2013**, *88*, 085117.
[46] T. L. Anderson, H. B. Krause, *Acta Crystallogr., Sect. B: Struct. Sci., Cryst. Eng. Mater.* **1974**, *30*, 1307.